Estimating Surfzone Currents with Near-Field Optical Remote Sensing

CIARA DOOLEY,[a,b] STEVE ELGAR,[a] BRITT RAUBENHEIMER,[a] AND LEVI GORRELL[a]

[a] *Woods Hole Oceanographic Institution, Woods Hole, Massachusetts*
[b] *Massachusetts Institute of Technology, Cambridge, Massachusetts*

(Manuscript received 30 January 2024, in final form 28 September 2024, accepted 14 November 2024)

ABSTRACT: Currents transport sediment, larvae, pollutants, and people across and along the surfzone, creating a dynamic interface between the coastal ocean and shore. Previous field studies of nearshore flows primarily have relied on relatively low spatial resolution deployments of in situ sensors, but the development of remote sensing techniques using optical imagery and naturally occurring foam as a flow tracer has allowed for high spatial resolution observations (on the order of a few meters) across the surfzone. Here, algorithms optical current meter (OCM) and particle image velocimetry (PIV) are extended from previous surfzone applications and used to estimate both cross-shore and alongshore 2-, 10-, and 60-min mean surface currents in the nearshore using imagery from both oblique and nadir viewing angles. Results are compared with in situ current meters throughout the surfzone for a wide range of incident wave heights, directions, and directional spreads. Differences between remotely sensed flows and in situ current meters are smallest for nadir viewing angles, where georectification is simplified. Comparisons of 10-min mean flow estimates from a nadir viewing angle with in situ estimates of alongshore and cross-shore currents had correlations $r^2 = 0.94$ and 0.51 with root-mean-square differences (RMSDs) = 0.07 and 0.16 m s^{-1} for PIV and $r^2 = 0.88$ and 0.44 with RMSDs = 0.08 and 0.22 m s^{-1} for OCM. Differences between remotely sensed and in situ cross-shore current estimates are at least partially owing to the difference between onshore-directed mass flux on the surface and offshore-directed undertow in the mid–water column.

KEYWORDS: Ocean dynamics; Coastal flows; Remote sensing; Field experiments

1. Introduction

Knowledge of surfzone fluid dynamics is necessary to understand the coastal environment. Bacteria, pollutants, larvae, and sediment are transported by currents near the shore, impacting beach safety, coastal morphology, and marine wildlife (Boehm 2003; Grant et al. 2005; Cowen et al. 2006; Halpern et al. 2008; Moulton et al. 2023). However, it is difficult to deploy and maintain many in situ sensors in the energetic environment of the surfzone (Holman and Haller 2013), and thus, many observational arrays have relatively large distances between instruments (e.g., most sensors > 20 m apart, with many separated by more than 50 m), limiting the spatial resolution of investigations. In contrast, analyzing sequences of remotely sensed images can provide high spatial resolution estimates of surfzone circulation patterns.

Algorithms applied to optical or infrared surfzone imagery determine mean surface currents by tracking the motion of naturally occurring foam and thermal signatures generated by breaking waves (Holland et al. 2001; Chickadel et al. 2003; Puleo et al. 2003; Perkovic et al. 2009; Holman and Haller 2013; Wilson et al. 2014; Dérian and Almar 2017; Anderson et al. 2021; Rodríguez-Padilla et al. 2021). Estimates of flows made with optical current meter (OCM; Chickadel et al. 2003) and particle image velocimetry (PIV; Raffel et al. 1998; Adrian 1991; Perkovic et al. 2009) algorithms compare favorably with in situ observations in tidal or riverine environments (Chickadel et al. 2011; Puleo et al. 2012; Jessup et al. 2013; Legleiter et al. 2017, 2020; McIlvenny et al. 2023) and in the swash or surfzone (Holland et al. 2001; Chickadel et al. 2003; Puleo et al. 2003; Perkovic et al. 2009; Wilson et al. 2014; Elgar et al. 2023). In the surfzone, PIV and OCM studies have focused on estimating alongshore currents (parallel to the shore), because estimating cross-shore (perpendicular to the shore) flows can be complex owing to wave rollers and breaking wave-driven shoreward mass transport, resulting in image-based estimates that may not be indicative of depth-averaged or subsurface cross-shore currents. Variations of the optical flow algorithm (Horn and Schunck 1981) have been proposed to estimate two-dimensional surfzone currents (Dérian and Almar 2017; Anderson et al. 2021; Rodríguez-Padilla et al. 2021), but comparisons with in situ current meters are limited.

Here, the OCM and PIV algorithms are optimized for tracking breaking-wave-induced foam in optical images to provide estimates of 2-, 10-, and 60-min mean cross-shore and alongshore surface flows in the surfzone. Velocity estimates from the two algorithms are compared with each other and with an extensive field dataset including measurements from twenty in situ sensors in cross-shore and alongshore transects. Differences between flow estimates from the nadir and oblique viewpoints are assessed.

2. Methods

a. Field observations

Field data were collected at the U.S. Army Corps of Engineers (USACE) Field Research Facility (FRF) on the Atlantic Ocean in Duck, North Carolina, during 2013 and 2022 (Fig. 1). Images were collected from stationary cameras mounted on a ~40-m-high tower (cross-shore and alongshore coordinates 34 and 585 m, respectively) overlooking the beach and from a

Corresponding author: Ciara Dooley, cdooley@whoi.edu

DOI: 10.1175/JTECH-D-24-0015.1

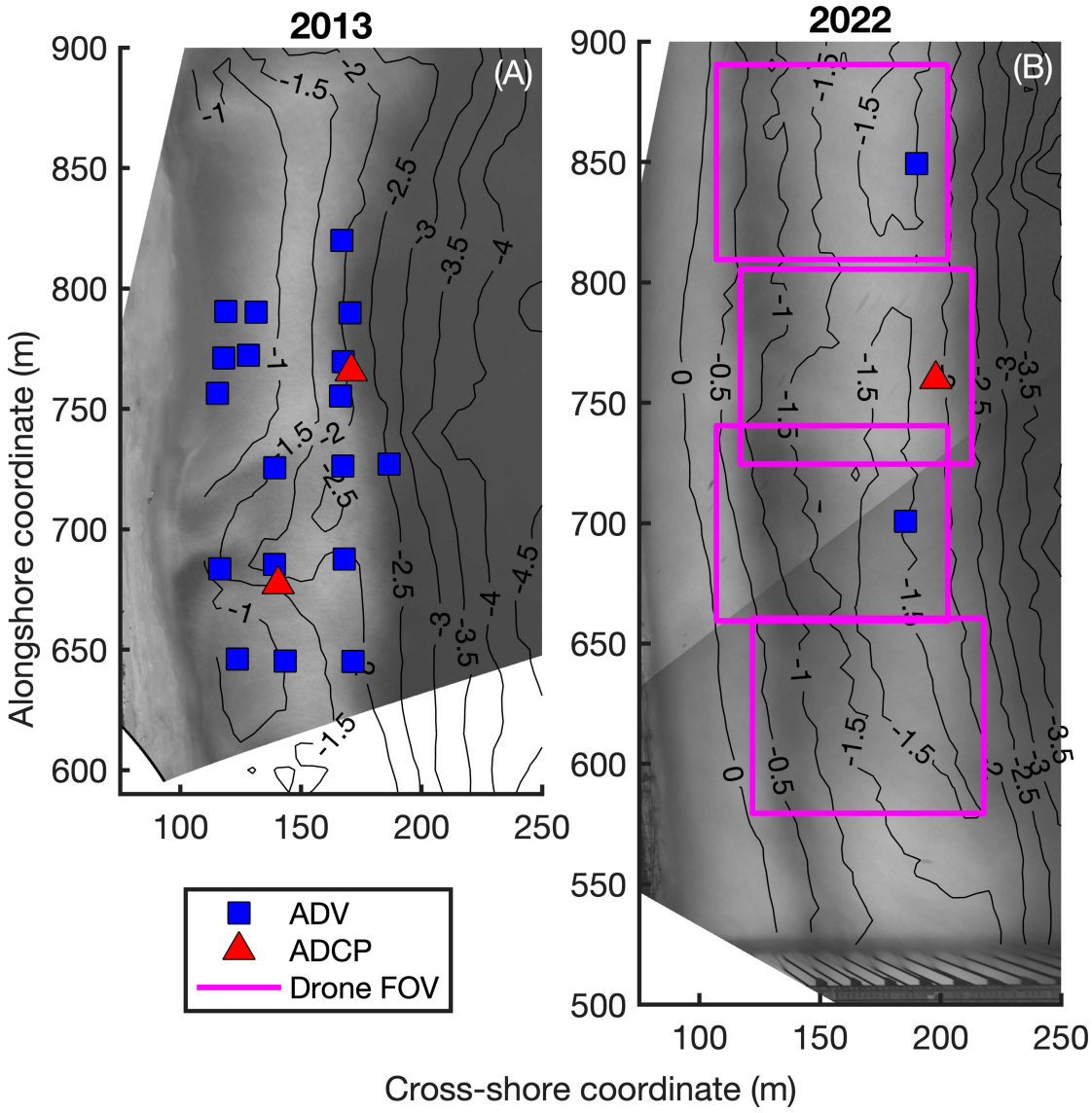

FIG. 1. Fields of view from a stationary camera mounted on a tower overlooking the beach (grayscale is a 10-min time-averaged image) and a drone camera (magenta boxes) and sensor locations as a function of cross-shore and alongshore coordinates for the (a) 2013 and (b) 2022 experiments at the FRF. Depth contours are drawn every 0.5 m. Symbols indicate in situ current profilers (ADCPs; red triangles) and velocimeters (ADVs; blue squares). Not all sensors were operational for the duration of each experiment. In the time-averaged image, lighter areas indicate foam caused by breaking waves. The vertical pilings of the FRF pier can be seen near $Y = 500$ m in (b). Remotely sensed current estimates were generated every 3.2 m in the cross-shore and alongshore across the entire field of view of the cameras (not shown).

drone flown over the surfzone. In situ currents were measured with acoustic Doppler current profilers (ADCPs) and acoustic Doppler velocimeters (ADVs) (Fig. 1). The bathymetry was surveyed intermittently throughout the experiments and ranged from nearly alongshore uniform (Fig. 1b) to alongshore inhomogeneous with rip channels, bumps, and holes (Fig. 1a). Incident wave conditions were measured with a wave buoy deployed in 17-m water depth (NOAA 44056) (Table 1, Fig. 2), and water levels and atmospheric conditions were measured near the end of the FRF pier (NOAA 8651370).

During 2013, image data were collected from a stationary camera during daylight hours (0800–1800 EDT) from 22 September to 24 October. During this period, 18 days had sufficient foam to derive current estimates (only data from image collections with significant wave heights greater than ~0.5 m were considered, with the cutoff height based on a visual inspection). In 2022, image data were collected from two stationary cameras on the tower (two cameras provide a wider field of view and current estimates in the overlapping area were averaged) and a drone-mounted camera (magenta boxes in Fig. 1b) for 23 flights (~20 mins each) over 5 days.

TABLE 1. Summary of wave conditions during imaging periods, measured in 17-m water depth.

Parameter	2013		2022	
	Min	Max	Min	Max
Significant wave height (m)	0.5	3.7	0.7	2.1
Peak period (s)	5.0	11.7	5.9	11.1
Wave direction relative to shore normal (°, positive from south)	−66	35	−38	31
Wave directional spread (°)	28	40	22	36

Remotely sensed current estimates were centered at locations every 3.2 m in the cross-shore and alongshore across the entire fields of view of the cameras.

Intrinsic camera calibrations were performed to correct for image distortion (Bouguet 2022), and the images from the tower-mounted cameras were georectified from an oblique field of view to a planar projection using surveyed ground control points (GCPs). The GPS antenna of a survey system was utilized as the target for GCPs. Imagery collected while vessels were transiting across the beach and surfzone during bathymetry and topography surveys provides hundreds of unique antenna locations (e.g., GCPs) across the camera field of view. Although selecting the locations of the vehicle GPS antenna in the image has error, using hundreds of GCPs results in a robust least squares fit of the rectification matrix. Pixels from rectified imagery were interpolated to a uniform grid with resolution dependent on the processing algorithm (see section 2 for more details). The drone-mounted camera utilized a nadir viewing angle and was geolocated using onboard postprocessed kinematic (PPK) GPS and an inertial navigation unit (there was limited visibility of the shoreline for fixed GCPs, and flights were not simultaneous with surveys). For both viewing angles, georectification assumed a flat sea surface at the mean measured sea level. Geolocation errors are discussed in section 4.

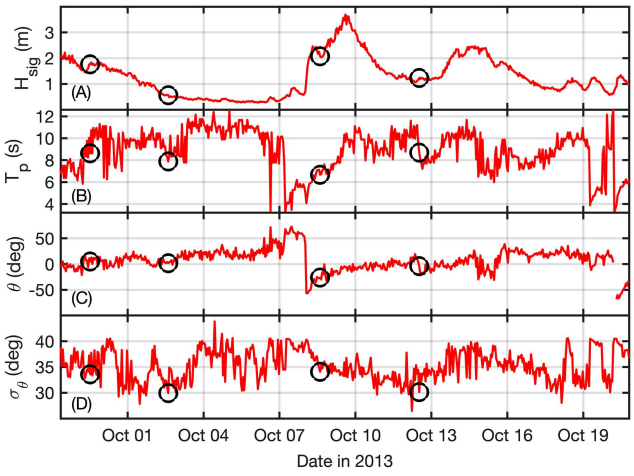

FIG. 2. (a) Significant wave height H_{sig}, (b) peak period T_p, (c) wave direction relative to shore normal θ (positive from the south), and (d) wave directional spread σ_θ measured in 17-m water depth vs time in 2013. Black circles indicate conditions corresponding to the remote sensing observations presented in Fig. 5.

b. *Remote sensing algorithms*

1) OPTICAL CURRENT METER

OCM estimates currents from the drift of foam over several seconds at a selected location (Chickadel et al. 2003). Algorithm parameters were adapted from the original application (Chickadel et al. 2003) to balance computation time and accuracy for the camera setup used here (Table 2), and new quality control techniques were applied to ensure sufficient foam was present in the image to act as a tracer for the current estimate. In addition, here the algorithm is applied in both the alongshore (e.g., Chickadel et al. 2003) and cross-shore directions.

To estimate a one-dimensional current (following Chickadel et al. 2003), image intensities along a 1-pixel-wide (0.2-m resolution) and 10-m-long row or column of pixels (a "pixel bar") are extracted from each image in a 20 s (window length) sequence of images sampled with an image frequency of 2 Hz. The pixel bars are stacked into a single image, creating a "timestack" that displays the chronological motion of foam at the location of that pixel bar (Fig. 3a). The timestacks are characterized by diagonal streaks demonstrating the distance foam has drifted over time, which is assumed to represent the velocity at the ocean surface at that location. The pixel intensity data of the timestack are Fourier transformed to provide a frequency (f)–wavenumber (k) spectrum (Fig. 3b) and converted to a velocity (v)–wavenumber spectrum using the mapping $v = f/k$ (Fig. 3c). This spectrum is integrated with respect to wavenumber, and the peak of the resultant velocity spectrum is an estimate of the current at the spatial location of the pixel bar (Fig. 3d). The original algorithm utilized a best-fit model of an idealized spectrum plus noise to find the estimate (Chickadel et al. 2003), but here selecting the peak

TABLE 2. OCM analysis parameters used by Chickadel et al. (2003) and here.

Parameter	Chickadel et al. (2003)	Adapted analysis
Alongshore resolution (m per pixel)	0.25	0.20
Cross-shore resolution (m per pixel)	0.45	0.20
Pixel bar length (m)	30	10
Image frequency (Hz)	2	2 (2022) 2.5 (2013)
Window length (s)	32	20
Step length (s)	16	10
Velocity bounds (m s^{-1})	[−3, 3]	[−2, 2]
Averaging period (min)	20	2, 10, 60

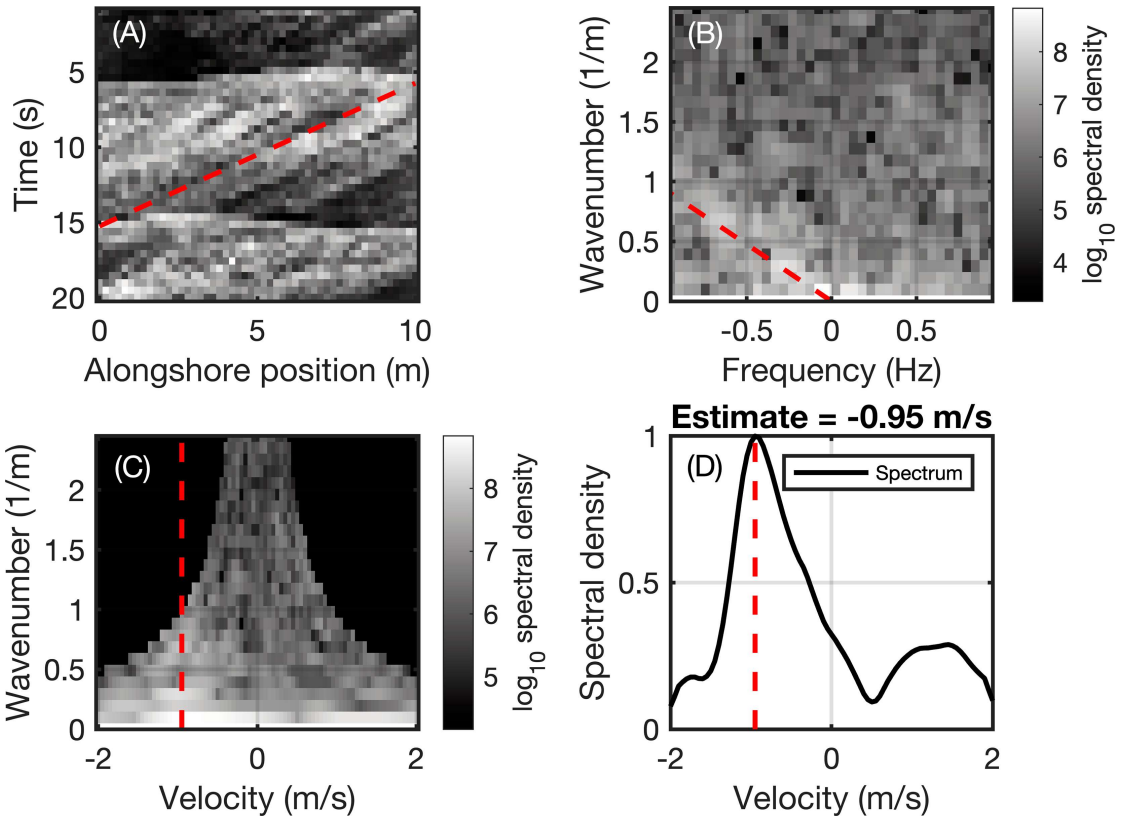

FIG. 3. The steps in the OCM method to determine a velocity estimate [similar to Figs. 2–5 in Chickadel et al. (2003), but for the data and approach used here]. (a) Image intensity as a function of time and alongshore position forming a timestack. The red dashed line highlights a foam streak advecting alongshore. (The horizontal lines are waves.) (b) Spectral density of image intensity (scale on right) as a function of wavenumber k and frequency f. The red dashed line through the high-energy values (lighter area) corresponds to the estimated velocity. (c) Spectral density of image intensity (scale on right) converted to a function of wavenumber and velocity v using $v = f/k$. The red dashed line through the high-energy values (lighter area) corresponds to the estimated velocity. (d) Spectral density of image intensity integrated over wavenumber vs velocity. The red dashed line through the spectral peak corresponds to the estimated velocity of -0.95 m s^{-1}.

of the spectrum yielded improved results. To avoid the signal of passing wave crests, the analysis was bounded to velocity magnitudes of 2 m s^{-1} maximum (wave celerities and group speeds are ~4–5 m s^{-1} in 2- to 3-m water depth).

To generate both cross-shore and alongshore current estimates, two timestacks are generated centered at the same location, using pixel bars at 90° angles. A pixel bar parallel to the shore will result in an alongshore estimate, whereas a pixel bar perpendicular to the shore will result in a cross-shore estimate. Estimate locations were spaced every 3.2 m in the alongshore and cross-shore, resulting in a 68% overlap between adjacent pixel bars. Estimates are temporally overlapped (step length; Table 2) by 10 s (50%).

2) PARTICLE IMAGE VELOCIMETRY

PIV estimates currents by determining the amount and direction that a small "window" within an image must be moved (Fig. 4) to maximize the correlation with the window in the previous image (Adrian 1991; Raffel et al. 1998), producing a single velocity estimate with cross-shore and alongshore components. The algorithm was applied using both DaVis 10 by LaVision and the open-source PIVlab (Thielicke and Stamhuis 2014; Thielicke and Sonntag 2021) algorithm in MATLAB. In both applications, the multipass FFT PIV algorithm was utilized with identical algorithm parameters (Table 3). The subpixel fit scheme utilized a three-point Gaussian fit, and no peak-locking reduction was employed. Results from DaVis 10 and PIVlab are nearly identical [$r^2 > 0.97$ and root-mean-square differences (RMSDs) < 0.04 m s^{-1} for 60-min mean estimates of cross-shore and alongshore flows], and results from both algorithms are used here.

To avoid the dominant signal of wave celerity from corrupting the mean current estimates, the final-pass PIV window size (3.2 m × 3.2 m) and image sample rate (1 Hz, obtained by downsampling the raw imagery) were selected to yield poor correlations between images when bores are present in a given window. Estimates with poor correlations are then filtered out during quality control. Foam at the bore crest is disorganized and does not maintain a coherent pattern over a 1-s period, and the small area of the final-pass window is insufficient for the larger scale signal of the passing bore to dominate, resulting in the observed drop in correlation relative to

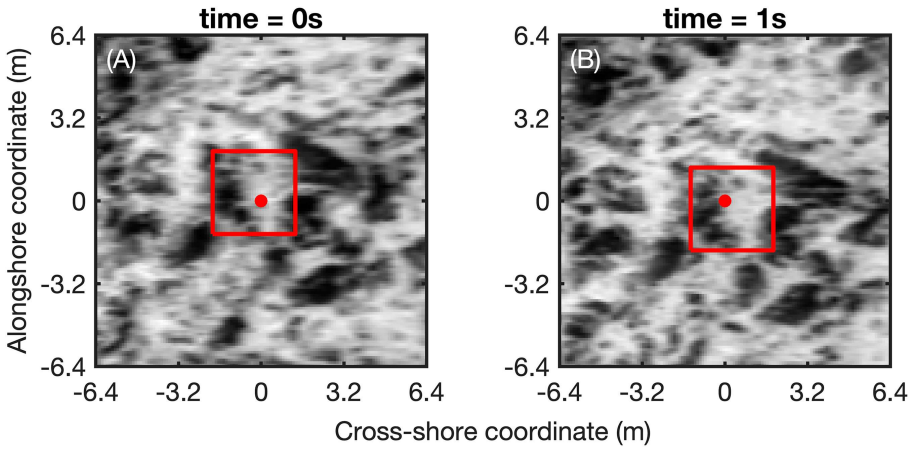

FIG. 4. Image intensity as a function of cross-shore and alongshore distance at (a) time = 0 and (b) time = 1 s. The PIV method estimates the velocity within the 3.2 m × 3.2 m window (red box) by determining the amount and direction of movement required to maximize the correlation between the images. The red dot marks the origin of the coordinate system, and the changing location of the red box between (a) and (b) indicates the advection of foam (light colors) in the cross-shore and alongshore directions.

sample areas without bores present. Algorithm parameters (e.g., pixel resolution, sample rate, window size, number of passes, and overlap between windows) were selected to balance computational time and accuracy for the camera setup used here (Table 3).

3) QUALITY CONTROL

The primary source of erroneous velocity estimates for both algorithms is insufficient foam tracer over the sample area or analysis period. To ensure sufficient foam was present to generate an estimate, quality control parameters were applied to both techniques. In addition, several techniques to preprocess imagery to improve measurement quality were evaluated [contrast limited adaptive histogram equalization (CLAHE), high-pass filtering, and intensity capping], but did not result in improved accuracy for this dataset (Thielicke and Stamhuis 2014).

To remove poor-quality OCM timestacks, the skewness, entropy, and variance of pixel intensities in each individual timestack were calculated, compared with a fixed threshold [<2 and >6 (dimensionless) and >100 (pixel intensity^2), respectively, for 2013 data], and estimates were rejected if they did not meet all criteria. In addition, all estimates offshore of the outer edge of the surfzone, identified by a relative drop in timestack variance in the cross-shore direction, were eliminated, reducing errors associated with "false positives" of high variance in pixel intensities due to light reflected from a rough sea surface instead of foam. In the time-averaged images, lighter areas indicate foam caused by breaking waves (Fig. 1). Typically, timestacks of high variance and entropy and low skewness are associated with these foamy areas, and thus, thresholds for the camera setup can be established. However, thresholds for filtering must be determined manually for each camera setup (varying color bit depth and camera exposure settings result in different "good" ranges of pixel intensities) by plotting timestack characteristics (skewness, entropy, and variance) and time-averaged images of pixel intensity as a function of cross-shore and alongshore coordinates for different sea surface lighting conditions. For example, depending on the camera setup and pixel intensities, the variance threshold can vary by several orders of magnitude.

TABLE 3. PIV analysis parameters.

Analysis parameter	Value applied
Alongshore resolution (m per pixel)	0.10
Cross-shore resolution (m per pixel)	0.10
Sample rate (Hz)	1
First-pass window size (m)	12.8 × 12.8
Second-pass window size (m)	6.4 × 6.4
Third-pass window size (m)	3.2 × 3.2
Fourth-pass window size (m)	3.2 × 3.2

To eliminate incorrect PIV estimates, results were rejected if the correlation coefficient (Raffel et al. 1998) between two windows was too low (<0.5) or if the variance of the image intensity of the analysis window was too low (i.e., sufficient foam was not present in the image). To account for variable sea surface conditions and lighting, the minimum variance threshold required was set as 4 times the average of the lowest 5% of the variances in all windows across the surfzone image (assumes spatial coverage of foam is $<95\%$).

Many PIV or OCM estimates may be discarded during this process, resulting in temporally and spatially patchy estimates. The percentage of estimates discarded was highly variable, depending on wave, bathymetry, and lighting conditions on a given day. Therefore, when calculating 2-, 10-, or 60-min mean currents, a minimum of 10% of the estimates across the average interval were required to pass quality control, and only passing values were used in the calculation of the mean. Increasing this threshold does not significantly reduce errors,

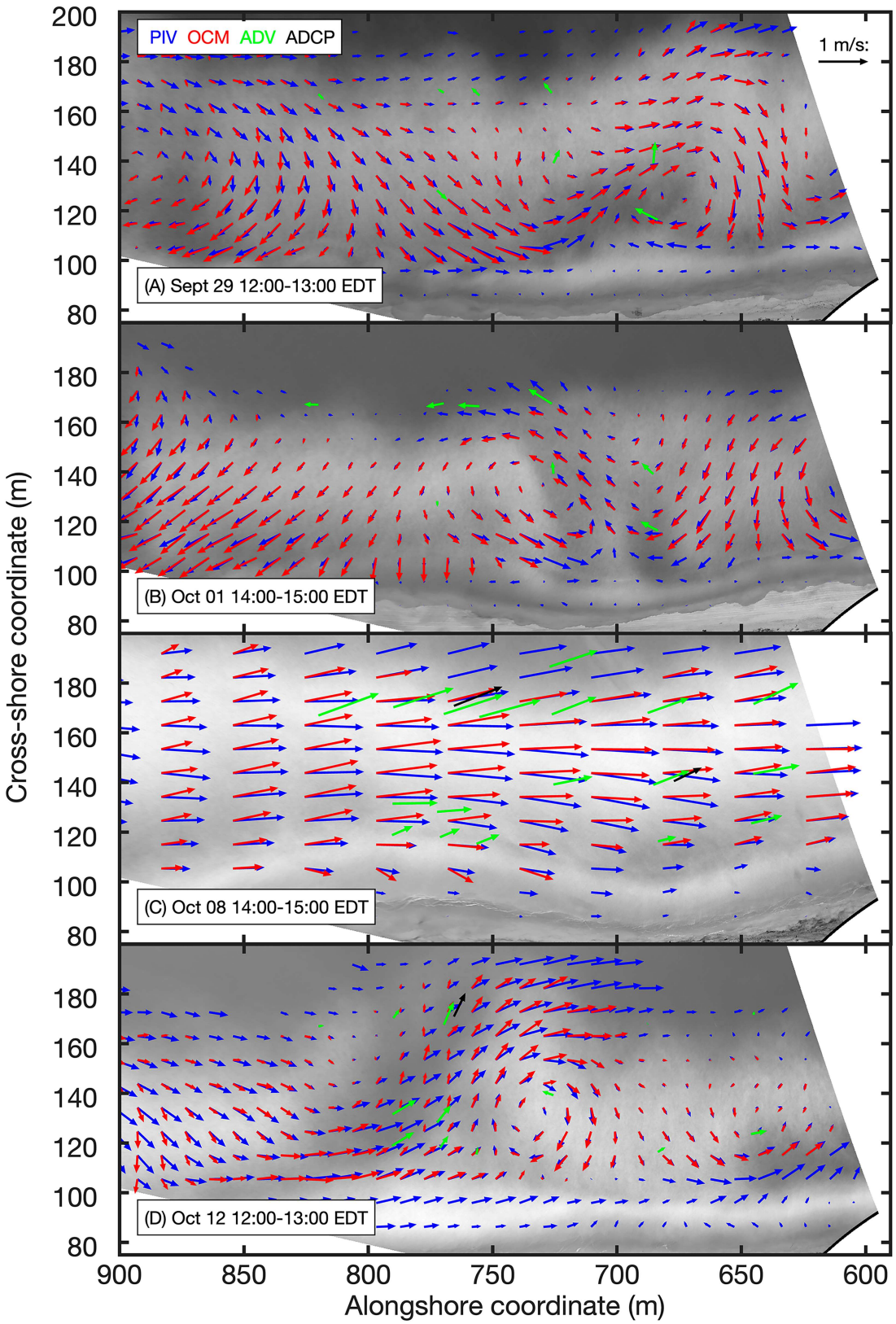

FIG. 5. Estimates of 60-min mean surface currents as a function of cross-shore and alongshore coordinates on (a) 29 Sep, (b) 1 Oct, (c) 8 Oct, and (d) 12 Oct 2013 (hours are listed on the figure) using OCM (red arrows point in the direction of flow with length proportional to speed) and PIV (blue arrows), and corresponding mid–water column measurements using ADVs (green arrows) and an ADCP (black arrows; deployed on 4 Oct). The spatial density of remote sensing estimates has been reduced in both the cross-shore and alongshore as a visual aid (originally every 3.2 m). The current arrows are superimposed on a 60-min time average of image data, with lighter areas indicating foam caused by breaking waves. Discussion and maps of the bathymetry for the four cases shown can be found in Elgar et al. 2023.

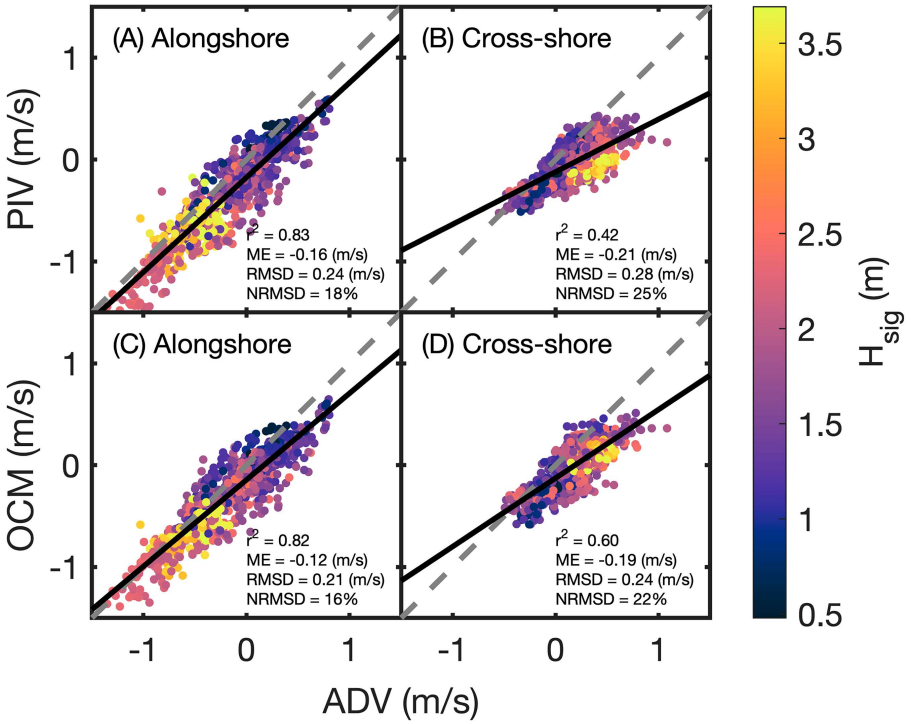

FIG. 6. 60-min mean surfzone currents estimated with (a),(b) PIV and (c),(d) OCM vs currents measured with in situ sensors for (a),(c) alongshore and (b),(d) cross-shore flows. Colors correspond to the significant wave height H_{sig} (color scale on the right, with purple indicating smaller waves and yellow indicating larger waves). Solid lines are linear least squares best fits, and the dashed lines are 1 to 1 correspondence. The correlation, ME (negative values correspond to an onshore or southward bias in remote sensing estimates of cross-shore and alongshore flows, respectively), RMSD, and normalized RMSD (NRMSD; normalized by the maximum in situ flow) are listed in each panel. Negative values are alongshore flows to the south and cross-shore flows toward the shore. There are 930 PIV and 851 OCM 60-min estimates.

so a low value was selected to maximize algorithm coverage. Limiting estimates to periods with adequate foam results in a sampling bias, but results were not associated with a specific phase of a passing wave, and resampling did not yield a more accurate result.

Error also is introduced by the selected sampling period and spatial extent of both algorithms. Larger spatial areas and faster sampling periods generally result in an improved signal-to-noise ratio but generate results over scales that may be inappropriate for the processes observed (e.g., estimating wave celerities instead of mean currents). Additionally, sampling to avoid the dominant signal of wave celerities (as done here) could lead to an underestimate of the mean surface current due to omitting the brief high-velocity signal at the wave crest.

For swash zone flows, where bores are moving more slowly and the sand is intermittently covered by run-up, both algorithms require different parameters than those used for surfzone applications. To prevent erroneous estimates in the swash, algorithm application was limited to water depths > 0.5 m (estimated from measured bathymetry and mean measured sea level) as wave celerities and group speeds are ~ 2 m s^{-1} in 0.5-m water depth, comparable with maximal mean flow estimates. After algorithm processing, mean velocities exceeding the range of expected maxima (2 m s^{-1} in the alongshore and 1 m s^{-1} in the cross-shore) were rejected.

TABLE 4. Correlations r^2 and RMSDs between remote sensing estimates (PIV and OCM) and in situ measurements for 2-, 10-, and 60-min mean flows in the surfzone.

	PIV vs in situ current meters				OCM vs in situ current meters			
	Alongshore		Cross-shore		Alongshore		Cross-shore	
	r^2	RMSD (m s^{-1})	r^2	RMSD (m s^{-1})	r^2	RMSD (m s^{-1})	r^2	RMSD (m s^{-1})
60 min	0.83	0.24	0.42	0.28	0.82	0.21	0.60	0.24
10 min	0.79	0.26	0.39	0.29	0.76	0.25	0.51	0.26
2 min	0.75	0.29	0.35	0.30	0.66	0.30	0.36	0.31

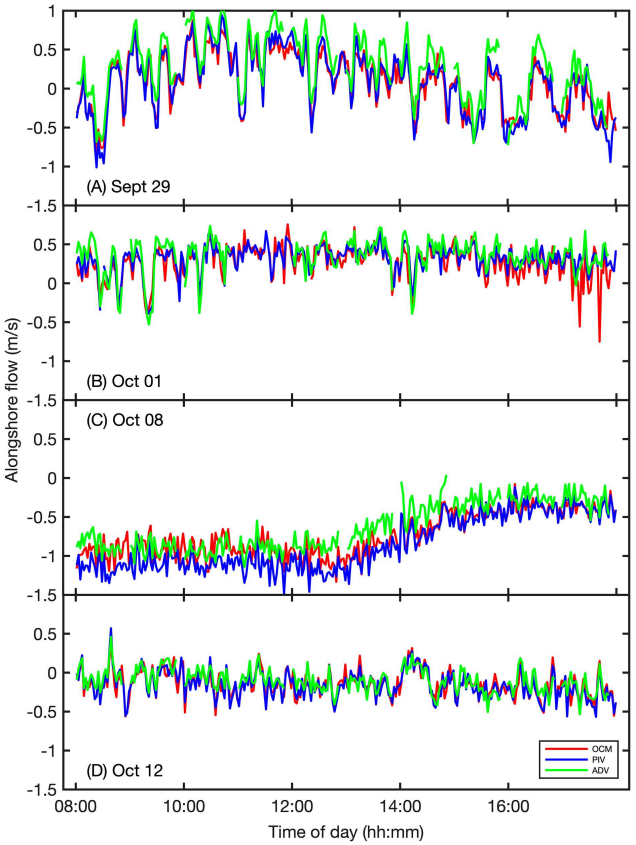

FIG. 7. Estimates of 2-min mean alongshore currents vs time on (a) 29 Sep, (b) 1 Oct, (c) 8 Oct, and (d) 12 Oct 2013 using OCM (red curves) and PIV (blue curves), and corresponding mid–water column currents measured with an ADV (green curves; located at cross-shore coordinate 116 m and alongshore coordinate 685 m). Gaps in the ADV time series are owing to low signal strength when not submerged continuously at low tide (Elgar et al. 2001, 2005).

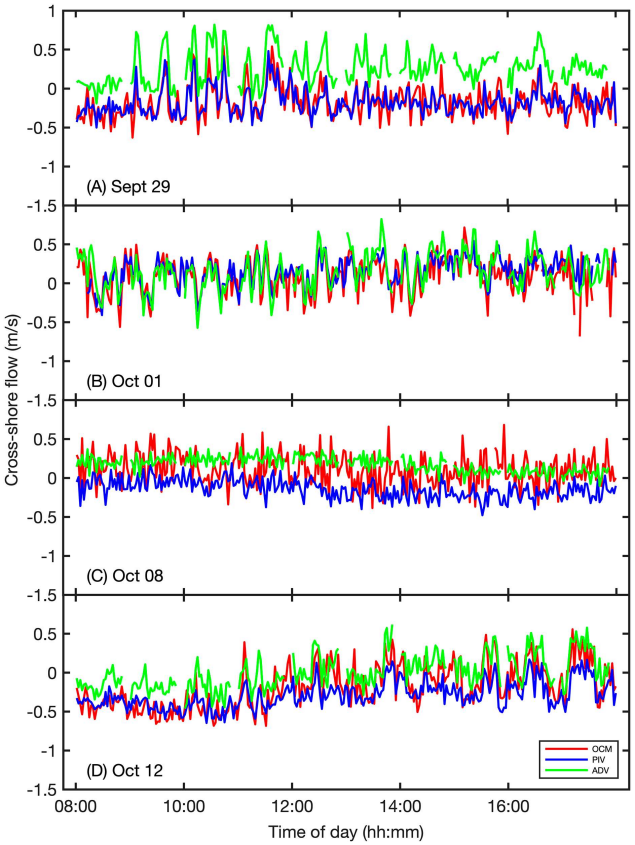

FIG. 8. Estimates of 2-min mean cross-shore currents vs time on (a) 29 Sep, (b) 1 Oct, (c) 8 Oct, and (d) 12 Oct 2013 using OCM (red curves) and PIV (blue curves), and corresponding mid–water column currents measured with an ADV (green curves; located at cross-shore coordinate 139 m and alongshore coordinate 725 m). Gaps in the ADV time series are owing to low signal strength when not submerged continuously at low tide (Elgar et al. 2001, 2005).

3. Remotely sensed flow estimates

During the 33-day observational period in 2013, the different wave conditions (Fig. 2) and bathymetries resulted in varying 60-min mean circulation patterns. Flows ranged from nearly alongshore uniform (Fig. 5c) when 2-m-high incident waves approached the surfzone from ~30° relative to shore normal (black circles in Fig. 2 for 8 October) to complex with eddies and rip-current-like offshore-directed currents (Figs. 5a,b,d) during smaller, more normally incident waves (black circles at the corresponding dates in Fig. 2). Magnitudes of 60-min mean alongshore flows (Fig. 5b) and eddy currents (Figs. 5a,c,d) are similar for PIV (blue arrows in Fig. 5) and OCM (red arrows in Fig. 5), with the strongest agreement closest to the location of the camera (alongshore coordinate 585 m, where viewing angle errors are lowest, discussed below).

The remotely sensed surface flows are similar to the mid–water column currents measured with in situ current meters (green arrows in Fig. 5 are ADVs, and the black arrows are from an upper bin of an ADCP), especially for alongshore-directed flows. Consistent with previous results (Church and Thornton 1993; Garcez Faria et al. 1998; and many others), there was little vertical variation in alongshore flows observed with the ADCPs, and here, the remotely sensed estimates of 60-min (Fig. 5) currents are highly correlated ($r^2 > 0.8$) with alongshore flows measured by the 20 in situ current meters (Fig. 6, Table 4). The remotely sensed estimate nearest each ADV (on a 3.2 m × 3.2 m grid) was used for comparison (locations are the same for both algorithms).

TABLE 5. Correlations r^2 and RMSDs between PIV and OCM for 2-, 10-, and 60-min mean flows in the surfzone. Estimates are compared at the locations of the in situ sensors.

	PIV vs OCM			
	Alongshore		Cross-shore	
	r^2	RMSD (m s^{-1})	r^2	RMSD (m s^{-1})
60 min	0.97	0.08	0.83	0.09
10 min	0.95	0.10	0.77	0.12
2 min	0.85	0.17	0.59	0.19

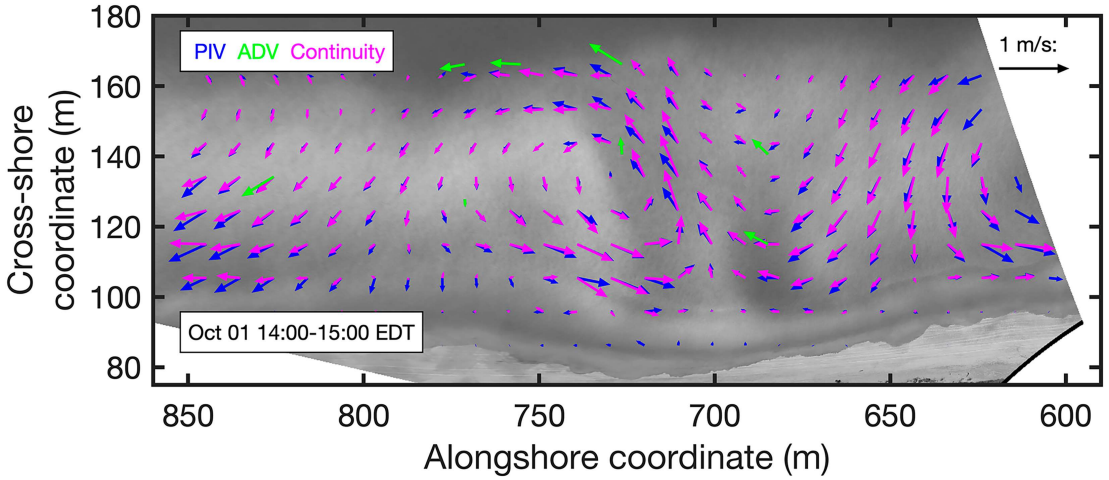

FIG. 9. The 60-min currents as a function of cross-shore and alongshore coordinates on 1 Oct estimated with PIV (surface flows; blue arrows point in the direction of flow with length proportional to speed), estimated with cross-shore currents synthesized using surveyed bathymetry (Fig. 1a), remotely sensed alongshore currents, and mass continuity (depth-averaged flows; magenta arrows), and measured with ADVs (green arrows in mid–water column). The spatial density of remote sensing estimates has been reduced in both the cross-shore and alongshore as a visual aid (originally every 3.2 m). The current arrows are superimposed on a 60-min time average of image data, with lighter areas indicating foam caused by breaking waves.

As the averaging time decreases from 60 to 2 min, the remote sensing estimates of alongshore currents become noisier, but remain correlated with in situ measurements ($r^2 \sim 0.7$ for 2-min means; Table 4), with similar long-period trends and higher-frequency fluctuations (Fig. 7). Residuals between remotely sensed and in situ currents are not correlated with any single-wave characteristic (significant wave height, radiation stress, wave direction, directional spread, and peak period), nor with bathymetric variability, suggesting that algorithm performance is not significantly affected by incident wave conditions or the underlying surfzone bathymetry. Bias between remotely sensed and in situ currents is onshore and to the south (Fig. 6), due to differences between surface and mid–water column flows and remote sensing errors (section 4).

In contrast with alongshore flows, it is not expected that cross-shore-directed surface flows always are the same as mid–water column cross-shore flows. For example, there can be shoreward propagating mass flux on the surface owing to breaking waves and a return flow (undertow) below the surface (Garcez Faria et al. 2000; and many others). Thus, although at times the mid–water column currents are similar to the remotely sensed surface circulation patterns (Figs. 5 and 8b,d), strong correlations between surface and mid–water column cross-shore flows are not expected nor observed in some cases (Table 4; Figs. 8a,c). Unlike most in situ sensors, remote sensing can estimate surface flows in the surfzone.

PIV and OCM estimates at the same locations (above the in situ sensor locations) are strongly correlated with each other, but not identical (Table 5). Differences between remotely sensed estimates may be attributable to the different length scales (10 m OCM and 3.2 m PIV) and sampling periods (20 s OCM and 1 s PIV), and the algorithm construction (section 2) of each technique because both methods use the same raw imagery and georectification parameters. Agreement

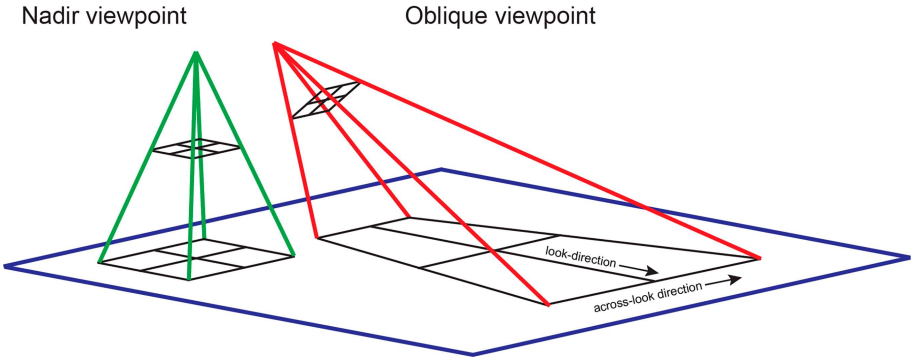

FIG. 10. Visualization (not to scale) of pixel sizes and stretching from nadir (green lines) and oblique (red lines) viewpoints. For a nadir viewpoint, distortion is minimized, whereas for an oblique viewpoint, pixels are elongated primarily along the along-look direction of the camera.

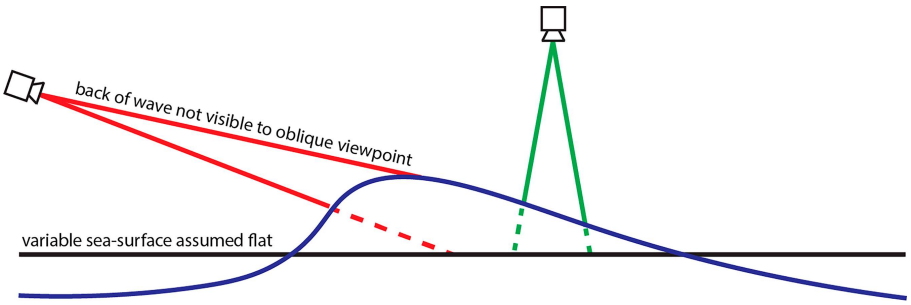

FIG. 11. Visualization (not to scale) of wave shadowing from an oblique viewpoint (red lines) and no shadowing from a nadir viewpoint (green lines).

is best closest to the camera location (Fig. 5), and the differences increase in the far field of view of the camera as pixel resolution decreases (discussed in section 4).

Assuming the remotely sensed alongshore currents are accurate and that the bathymetry is known, mass continuity can be used to estimate depth-averaged cross-shore currents (Holman and Haller 2013; Wilson et al. 2014). Here, high spatial resolution bathymetry measured on 2 October (Fig. 1a) was combined with remotely sensed 10- and 60-min mean alongshore currents to estimate depth-averaged cross-shore flows for two 10-h periods adjacent in time (1 and 2 October) to the survey. A cross-shore no-flow boundary condition was applied at the shoreline. Alongshore flows and bathymetry were spatially smoothed to help with model convergence. Some errors are introduced by the numerical method (least squares solver) and possibly by small changes in the bathymetry over the period surrounding the survey (~1 day). The depth-averaged flows produced by assuming continuity are nearly the same as remotely sensed surface flows at many locations (Fig. 9), suggesting surface and mid–water column cross-shore flows are similar. Depth-averaged continuity-based flows were similar to remotely sensed surface flows for all 20 1-h datasets (not shown).

4. Sources of error

Although quality control parameters reduce many errors associated with image quality and insufficient foam tracer, inaccurate estimates remain due to the noise inherent in sea surface imagery and geolocation errors. Additionally, oblique viewing angles introduce errors owing to georectification limitations (stretched pixels far from the camera and assumption of a flat sea surface) and decreasing image quality (blur, loss of contrast, and distortion) with increasing distance from the camera. These errors are investigated by comparisons of PIV and OCM flow estimates from images obtained from a nadir viewing angle (drone-mounted camera) with images obtained from oblique viewing angles (tower-mounted camera). The nadir viewing angle is used as ground truth in the comparison of 10- and 2-min mean flows (drone battery life limited flights to approximately 20 min). The same analysis parameters and quality control techniques were applied to nadir and oblique imagery.

The nadir viewing angle is assumed to be ground truth because it reduces several known sources of error:

1) Pixel distortion far from the camera. When viewing the ocean at an oblique angle, imagery in the far field of view of the camera becomes stretched in the camera look direction during georectification (Fig. 10), and spatial resolution decreases (pixels are larger). For the geometry and cameras used here, the nadir viewing angle provides georectified resolutions < 0.10 m per pixel across the entire field of view of the camera. In contrast, the oblique viewing angle provides georectified resolutions < 0.10 m per pixel in the near field of view, but pixel resolution is stretched to roughly 0.15 m $\times$ 0.75 m in the far field of view (approximately 300 m from the camera). Georectified pixels are interpolated to a uniform grid (e.g., 0.10 m per pixel) for algorithm processing, introducing error.
2) Reduced image quality at a distance. When compared with the camera near field of view, image quality in the far field of view deteriorates, reducing the clarity of foam tracer. Lens focal length, aperture, and shutter speed can be adjusted to optimize the image quality for a given camera setup, but under variable lighting conditions in the field, there is no ideal solution, particularly for a large field of view. A polarizing filter placed over the front-end

TABLE 6. Correlations r^2 and RMSDs between remote sensing techniques (PIV and OCM) and in situ measurements for 2- and 10-mean flows in the surfzone using a nadir viewing angle (drone imagery).

	Nadir PIV vs in situ current meters					Nadir OCM vs in situ current meters				
	Alongshore		Cross-shore			Alongshore		Cross-shore		
	r^2	RMSD (m s^{-1})	r^2	RMSD (m s^{-1})	Points	r^2	RMSD (m s^{-1})	r^2	RMSD (m s^{-1})	Points
10 min	0.94	0.07	0.51	0.16	23	0.88	0.08	0.44	0.22	19
2 min	0.91	0.08	0.42	0.19	134	0.81	0.11	0.31	0.28	113

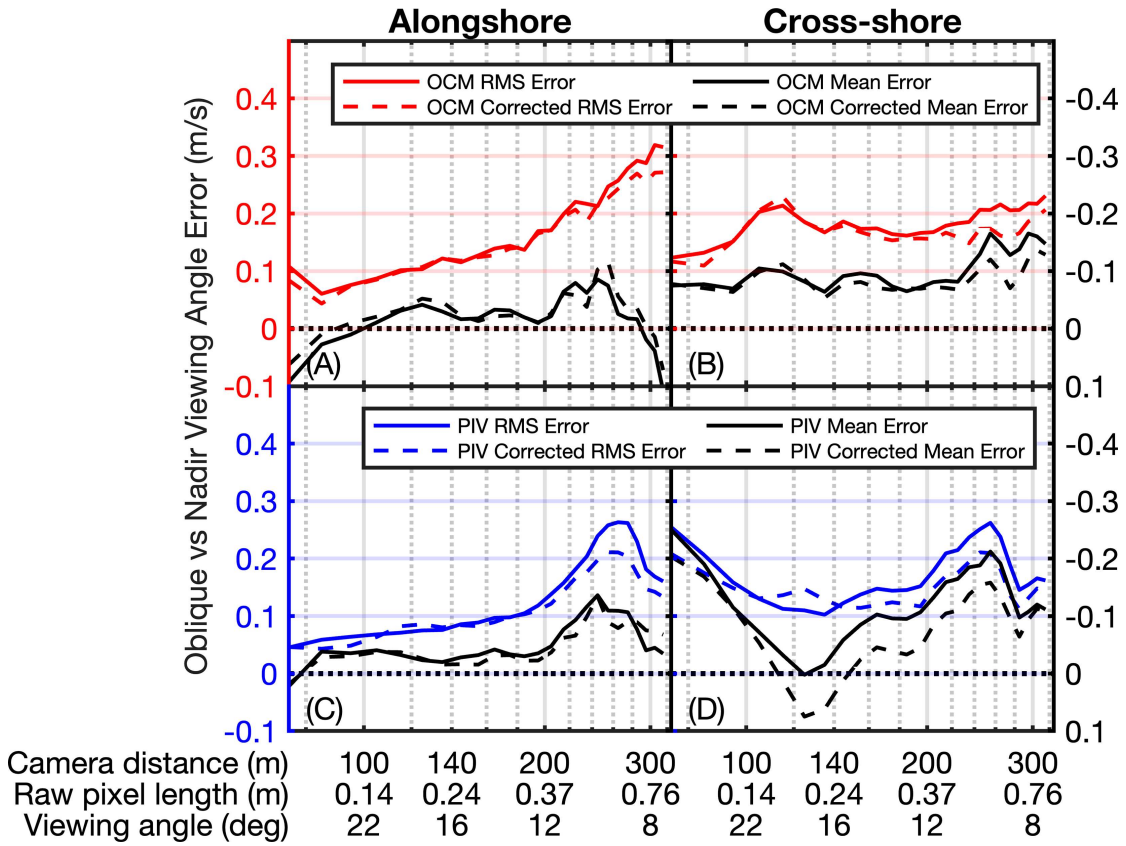

FIG. 12. RMS (red and blue curves; left axes) and mean (black curves; right axes) differences between remotely sensed 10-min mean flows estimated from oblique imagery and those from nadir imagery (assumed to be ground truth) vs camera distance, raw pixel length, and viewing angle of the tower camera for OCM in the (a) alongshore and (b) cross-shore directions and for PIV in the (c) alongshore and (d) cross-shore directions, with (dashed curves) and without (solid curves) pixel stretching correction. Camera distance is the horizontal distance between the tower camera and the flow location. Raw pixel length is the stretched dimension of image pixels elongated in the tower camera look direction. Viewing angle is the tilt of the tower camera look direction measured downward from horizontal. Negative MEs correspond to an onshore or southward bias in the oblique estimates of cross-shore and alongshore flows, respectively.

optics could help reduce ambient lighting variability, but this technique was not tried here. Images can be preprocessed before algorithm application to enhance contrast; however, adjustments (see section 2) did not improve the results here. When compared with the tower-mounted camera, the drone-mounted camera had significantly improved image quality and was closer to the surface of the ocean with a smaller field of view.

3) Sea-surface viewing angle bias. Georectification requires a known elevation for the projected surface. Here, the sea surface is assumed flat at the measured mean water elevation, a simplification that does not represent the complexity of shoreward propagating surface gravity waves. Waves move up and down, which can result in an apparent motion in the images when viewed from an oblique angle (Chickadel et al. 2003; Perkovic et al. 2009). For low viewing angles and tall waves, wave crests can obscure the sea surface behind them (wave shadowing; Fig. 11), resulting in an offshore flow bias due to the apparent offshore motion of the rising wave crest without the corresponding apparent onshore motion of the falling trough (Perkovic et al. 2009). A nadir viewing angle reduces apparent motion from rising and falling waves.

Geolocation errors can also be caused by errors in the estimated position of the camera. For the platforms utilized here and the flows observed, these errors are estimated to be small in the near field of view (<0.1 m s^{-1}). Assuming worst-case positioning errors (per manufacturer specifications), the drone-mounted camera is estimated to have a maximum 2.5-m spatial offset in rectified imagery with a negligible amount of added distortion. For complex circulation patterns, the median shear (change in velocity over distance) observed in 2-min mean estimates is $\sim$0.015 1 s^{-1}, indicating the worst-case 2.5-m spatial offset would result in a median error of $\sim$0.038 m s^{-1}. Although positional drift can induce an artificial flow, it is estimated to be small. Assuming worst-case drift during a 2-min period (the minimum averaging period of analysis) results in an additional error of $\sim$0.02 m s^{-1}. For the tower-mounted camera, previously unused GCPs were applied to check the camera rectification matrix and demonstrated $\sim$0.1-m spatial offsets in the

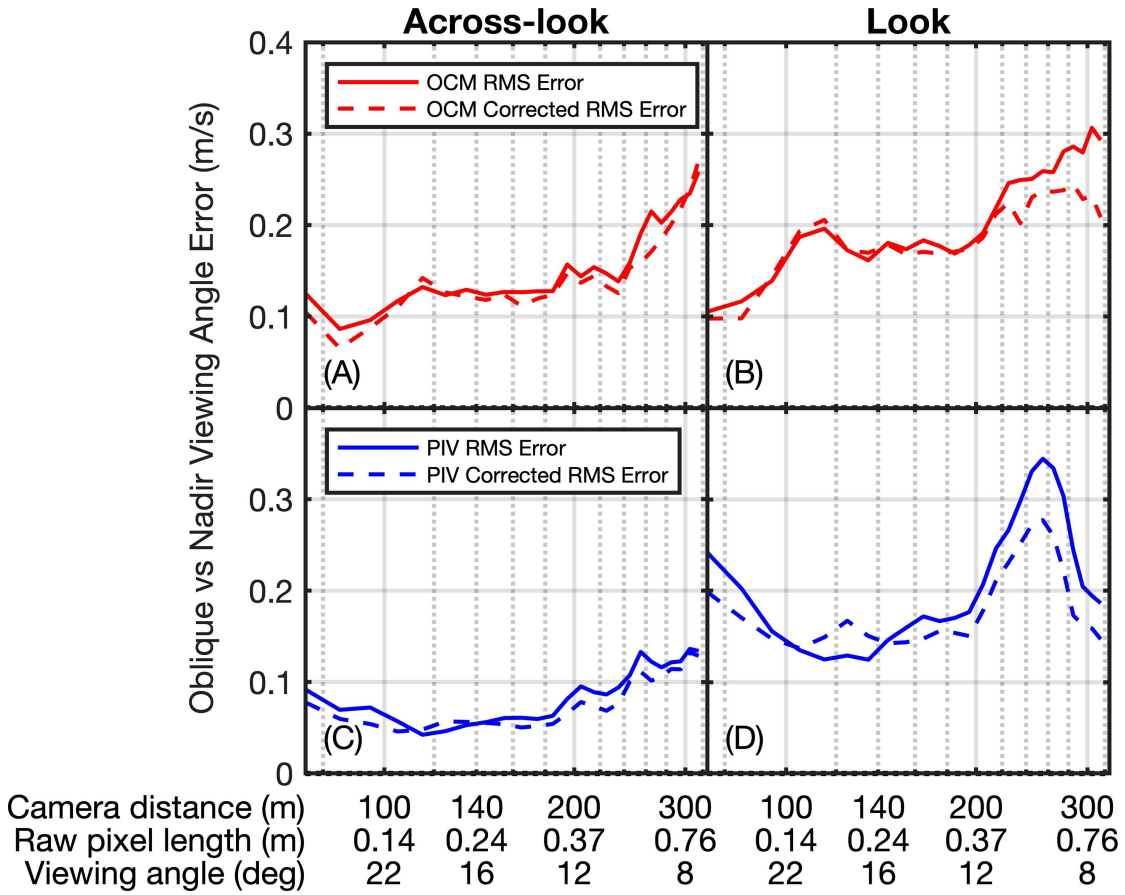

FIG. 13. RMS errors between remotely sensed 10-min mean flows estimated from oblique imagery and nadir imagery vs camera distance, raw pixel length, and viewing angle for OCM in the (a) across-look and (b) look directions and for PIV in the (c) across-look and (d) look directions, with (dashed curves) and without (solid curves) pixel stretching correction. Camera distance is the horizontal distance between the camera and the flow location. Raw pixel length is the stretched dimension of image pixels elongated in the camera look direction. Viewing angle is the tilt of the look direction measured downward from horizontal.

rectified imagery in the near field of view (<150 m from the camera), resulting in negligible impacts to velocity estimates. However, in the far field of view, where near-grazing angles occur, small changes in tilt due to camera vibrations could contribute significantly to errors.

Alongshore surface flow estimates from the nadir drone imagery are highly correlated ($r^2 \sim 0.9$) with mid–water column in situ measurements for 10-min means (Table 6). Cross-shore flows are less correlated ($r^2 \sim 0.5$), in part due to differences between surface flows and mid–water column flows (discussed in section 3). Correlations are somewhat reduced for 2-min means (Table 6). RMSDs with in situ sensors are smaller with a nadir field of view (Table 6) than with an oblique field of view (Table 4; 10- and 2-min mean estimates).

Currents estimated with the tower-mounted camera were compared with corresponding estimates from the drone-mounted camera at every 3.2 m × 3.2 m location during the 2022 experiment (Figs. 1b and 12). For both PIV (Figs. 12a,b) and OCM (Figs. 12c,d), RMS errors relative to the nadir view typically increase with distance from the tower camera and with viewing angle, and errors often are higher in the cross-shore than in the alongshore. Residuals are not correlated with any single wave characteristic (significant wave height, radiation stress, wave direction, directional spread, and peak period) (2022 data; Table 1).

To assess the contribution of pixel stretching in the far field to the observed differences between nadir and oblique viewing angles, the high spatial resolution drone images were reprojected, and the pixels averaged together to appear as if viewed from the tower camera. These altered images were processed with both PIV and OCM, resulting in flows with errors due to interpolating across stretched pixels (similar to the original tower images), but no errors due to reduced image quality at distance or sea surface viewing angle bias. Flows estimated from the tower images are then "corrected" by subtracting the difference in flows estimated from the reprojected nadir images and original nadir images, removing error attributed to pixel stretching (dashed curves in Fig. 12). For both algorithms, applying this correction had little effect on errors between the two viewpoints (Fig. 12; compare solid with dashed curves), suggesting pixel stretching is not the primary source of error.

To investigate further the impacts of the camera angle on errors, flows were deconstructed into a local coordinate

system based on the camera viewing angle, consisting of camera look direction and across-look direction components (see visualization in Fig. 10). For both OCM (Figs. 13a,b) and PIV (Figs. 13c,d) flow estimates, errors are predominantly in the camera look direction (i.e., in the direction of stretched pixels) and typically increase with distance from the camera. Removing errors attributed to pixel stretching (dashed curves in Fig. 13) does not have a significant impact on errors in either the look or the across-look direction. This suggests errors primarily are related to the camera setup with regard to reduced image quality at distance, geolocation errors at near-grazing angles, or sea surface viewing angle bias.

Results also were decomposed based on the angle (aligned or unaligned with camera viewing angle) and type of flow (predominantly cross-shore or predominantly alongshore) (not shown). Cross-shore and alongshore flows both had larger look direction errors, with the highest magnitude errors occurring when estimated flows were aligned with the look direction of the camera (flow in the low-resolution direction of stretched pixels). A large peak in PIV look direction error (Fig. 13d, ~260 m from the camera) corresponds to a significant underestimate of a strong offshore and northward flow aligned with the camera look direction (the same peak is noticeable in cross-shore and alongshore estimates; Figs. 12c,d).

Differences in error distributions between OCM and PIV are attributable to the different length scales (10 m OCM and 3.2 m PIV) and sampling periods (20 s OCM and 1 s PIV) and the algorithm construction (section 2) of each technique. Despite application to the same imagery over identical averaging periods, differences in the error distributions can be significant, particularly at distances far from the camera (Fig. 13). For surfzone flow estimates, OCM results are overall noisier than PIV results (Figs. 12 and 13) but, perhaps due to using longer sampling periods and longer length scales, are more consistent when interpolating across low-resolution data (no peaks in OCM errors; Figs. 13a,b).

To correct for errors from sea surface elevation assumptions, some analyses have applied a theoretical model to account for wave shadowing (Perkovic et al. 2009), correcting for an offshore bias in the cross-shore flow. Here, mean errors (MEs) in the cross-shore flows (black curves, Fig. 12) show an onshore bias from the oblique viewing angle, indicating that wave shadowing is not a significant source of error. This disparity is hypothesized to be due to the assumptions in the shadowing model that waves are sinusoidal with foam tracer evenly distributed across the wave front and back. Here, surfzone waves break and become bores, and foam on the bore front is disorganized and only resolves into traceable patterns on the back of the wave. Opposite to the wave shadowing model, foam is viewed primarily on a falling sea surface, inducing an apparent onshore motion and bias (Chickadel et al. 2003). Using a sawtooth wave shape and a discontinuous finite jump in tracer as the theoretical model for sea surface elevation (Chickadel et al. 2003) corrects for an onshore bias, but does not decrease errors overall, likely due to other assumptions in the model (incident wave direction and saturated surfzone wave heights that are a constant fraction of the local depth based on estimated bathymetry).

5. Conclusions

High spatial resolution (3.2 m × 3.2 m) surface flows in the surfzone were estimated with remote sensing by applying the optical current meter (OCM) and particle image velocimetry (PIV) algorithms to rapidly (1–2 Hz) sampled images of the sea surface. Remote sensing estimates of alongshore-directed currents are correlated ($r^2 > 0.8$–0.9 for 60-min mean flows) with currents measured with in situ current meters deployed in the mid–water column. Remotely sensed cross-shore currents are less correlated with mid–water column flows, likely partially owing to differences between shoreward propagating mass flux on the surface and offshore-directed undertow in mid–water column, as well as error introduced by noise from breaking incident waves. Remotely sensed currents become less accurate with distance away from the camera and with an increasing oblique view of the sea surface. A camera with a nadir viewing angle (e.g., from a drone) can yield more accurate results than a camera viewing the water surface from an oblique angle. However, when a fixed camera with an oblique viewing angle is required (perhaps due to inclement weather, the need for a longer time series, or air–space restrictions), higher viewing angles and smaller distances between the surface of interest and the camera location result in smaller errors owing to loss of image quality, georectification limitations, and sea surface viewing angle bias. In addition, using multiple cameras with overlapping fields of view from different viewing angles can increase confidence in current estimates given the difficulty in estimating errors.

Acknowledgments. We thank the FRF and PVLAB field crews for helping to deploy, maintain, and recover sensors and perform bathymetric surveys in difficult surfzone conditions, Dr. David Clark and Dr. Jeff Hansen for helping propose, design, and manage the 2013 field experiment, and Dr. Melissa Moulton for valuable discussions. Funding was provided by the National Science Foundation, National Security Science and Engineering and Vannevar Bush Faculty Fellowships, a National Defense Science and Engineering Graduate Fellowship, and a WHOI Independent Study award.

Data availability statement. The 2013 surfzone data can be found in Elgar and Raubenheimer (2019) at https://doi.org/10.17603/ds2-c9p4-7264, the 2022 surfzone data can be found in Elgar and Raubenheimer (2022) at https://doi.org/10.17603/ds2-1vvz-nc16, and incident wave conditions and bathymetric surveys can be found on the FRF THREDDS server at https://chlthredds.erdc.dren.mil/thredds/catalog/frf/catalog.html under oceanography and geomorphology. The raw image files (over 3 TB) can be accessed via discussions with the authors.

REFERENCES

Adrian, R. J., 1991: Particle-imaging techniques for experimental fluid mechanics. *Annu. Rev. Fluid Mech.*, **23**, 261–304, https://doi.org/10.1146/annurev.fl.23.010191.001401.

Anderson, D., A. S. Bak, K. L. Brodie, N. Cohn, R. A. Holman, and J. Stanley, 2021: Quantifying optically derived two-

dimensional wave-averaged currents in the surf zone. *Remote Sens.*, **13**, 690, https://doi.org/10.3390/rs13040690.

Boehm, A. B., 2003: Model of microbial transport and inactivation in the surf zone and application to field measurements of total coliform in Northern Orange County, California. *Environ. Sci. Technol.*, **37**, 5511–5517, https://doi.org/10.1021/es034321x.

Bouguet, J.-Y., 2022: Camera calibration toolbox for matlab (1.0). CaltechDATA, https://doi.org/10.22002/D1.20164.

Chickadel, C. C., R. A. Holman, and M. H. Freilich, 2003: An optical technique for the measurement of longshore currents. *J. Geophys. Res.*, **108**, 3364, https://doi.org/10.1029/2003JC001774.

——, S. A. Talke, A. R. Horner-Devine, and A. T. Jessup, 2011: Infrared-based measurements of velocity, turbulent kinetic energy, and dissipation at the water surface in a tidal river. *IEEE Geosci. Remote Sens. Lett.*, **8**, 849–853, https://doi.org/10.1109/LGRS.2011.2125942.

Church, J. C., and E. B. Thornton, 1993: Effects of breaking wave induced turbulence within a longshore current model. *Coastal Eng.*, **20** (1–2), 1–28, https://doi.org/10.1016/0378-3839(93)90053-B.

Cowen, R. K., C. B. Paris, and A. Srinivasan, 2006: Scaling of connectivity in marine populations. *Science*, **311**, 522–527, https://doi.org/10.1126/science.1122039.

Dérian, P., and R. Almar, 2017: Wavelet-based optical flow estimation of instant surface currents from shore-based and UAV videos. *IEEE Trans. Geosci. Remote Sens.*, **55**, 5790–5797, https://doi.org/10.1109/TGRS.2017.2714202.

Elgar, S., and B. Raubenheimer, 2019: Surf zone vorticity and advection (RODSEX) field experiment. DesignSafe-CI, https://doi.org/10.17603/ds2-c9p4-7264.

——, and ——, 2022: Surfzone energy cascades: Alongshore array of current meters and pressure gages in 2 m depth, and one gage in ~1 m depth, Duck, NC. DesignSafe-CI, https://doi.org/10.17603/ds2-1vvz-nc16.

——, ——, and R. T. Guza, 2001: Current meter performance in the surf zone. *J. Atmos. Oceanic Technol.*, **18**, 1735–1746, https://doi.org/10.1175/1520-0426(2001)018<1735:CMPITS>2.0.CO;2.

——, ——, and ——, 2005: Quality control of acoustic Doppler velocimeter data in the surfzone. *Meas. Sci. Technol.*, **16**, 1889–1893, https://doi.org/10.1088/0957-0233/16/10/002.

——, C. Dooley, L. Gorrell, and B. Raubenheimer, 2023: Observations of two-dimensional turbulence in the surfzone. *Phys. Fluids*, **35**, 085142, https://doi.org/10.1063/5.0159170.

Garcez Faria, A. F., E. B. Thornton, T. P. Stanton, C. V. Soares, and T. C. Lippmann, 1998: Vertical profiles of longshore currents and related bed shear stress and bottom roughness. *J. Geophys. Res.*, **103**, 3217–3232, https://doi.org/10.1029/97JC02265.

——, ——, T. C. Lippmann, and T. P. Stanton, 2000: Undertow over a barred beach. *J. Geophys. Res.*, **105**, 16 999–17 010, https://doi.org/10.1029/2000JC900084.

Grant, S. B., J. H. Kim, B. H. Jones, S. A. Jenkins, J. Wasyl, and C. Cudaback, 2005: Surf zone entrainment, along-shore transport, and human health implications of pollution from tidal outlets. *J. Geophys. Res.*, **110**, C10025, https://doi.org/10.1029/2004JC002401.

Halpern, B. S., and Coauthors, 2008: A global map of human impact on marine ecosystems. *Science*, **319**, 948–952, https://doi.org/10.1126/science.1149345.

Holland, K. T., J. A. Puleo, and T. N. Kooney, 2001: Quantification of swash flows using video-based particle image velocimetry. *Coastal Eng.*, **44**, 65–77, https://doi.org/10.1016/S0378-3839(01)00022-9.

Holman, R., and M. C. Haller, 2013: Remote sensing of the nearshore. *Annu. Rev. Mar. Sci.*, **5**, 95–113, https://doi.org/10.1146/annurev-marine-121211-172408.

Horn, B. K. P., and B. G. Schunck, 1981: Determining optical flow. *Artif. Intell.*, **17**, 185–203, https://doi.org/10.1016/0004-3702(81)90024-2.

Jessup, A. T., C. C. Chickadel, S. A. Talke, and A. R. Horner-Devine, 2013: Cohstrex: Coherent structures in rivers and estuaries experiment. *Coherent Flow Structures at Earth's Surface*, J. G. Venditti, J. L. Best, M. Church, and R. J. Hardy, Eds., Wiley, 215–230.

Legleiter, C. J., P. J. Kinzel, and J. M. Nelson, 2017: Remote measurement of river discharge using thermal Particle Image Velocimetry (PIV) and various sources of bathymetric information. *J. Hydrol.*, **554**, 490–506, https://doi.org/10.1016/j.jhydrol.2017.09.004.

——, T. Pavelsky, M. Durand, G. Allen, A. Tarpanelli, R. Frasson, I. Guneralp, and A. Woodget, 2020: *Remote Sensing of Flow Velocity, Channel Bathymetry, and River Discharge*. MDPI, 286 pp.

McIlvenny, J., B. J. Williamson, I. A. Fairley, M. Lewis, S. Neill, I. Masters, and D. E. Reeve, 2023: Comparison of dense optical flow and PIV techniques for mapping surface current flow in tidal stream energy sites. *Int. J. Energy Environ. Eng.*, **14**, 273–285, https://doi.org/10.1007/s40095-022-00519-z.

Moulton, M., S. H. Suanda, J. C. Garwood, N. Kumar, M. R. Fewings, and J. M. Pringle, 2023: Exchange of plankton, pollutants, and particles across the nearshore region. *Annu. Rev. Mar. Sci.*, **15**, 167–202, https://doi.org/10.1146/annurev-marine-032122-115057.

Perkovic, D., T. C. Lippmann, and S. J. Frasier, 2009: Longshore surface currents measured by Doppler radar and video PIV techniques. *IEEE Trans. Geosci. Remote Sens.*, **47**, 2787–2800, https://doi.org/10.1109/TGRS.2009.2016556.

Puleo, J. A., G. Farquharson, S. J. Frasier, and K. T. Holland, 2003: Comparison of optical and radar measurements of surf and swash zone velocity fields. *J. Geophys. Res.*, **108**, 3100, https://doi.org/10.1029/2002JC001483.

——, T. E. McKenna, K. T. Holland, and J. Calantoni, 2012: Quantifying riverine surface currents from time sequences of thermal infrared imagery. *Water Resour. Res.*, **48**, W01527, https://doi.org/10.1029/2011WR010770.

Raffel, M., C. E. Willert, F. Scarano, C. J. Kähler, S. T. Wereley, and J. Kompenhans, 1998: *Particle Image Velocimetry: A Practical Guide*. Springer, 253 pp.

Rodríguez-Padilla, I., B. Castelle, V. Marieu, P. Bonneton, A. Mouragues, K. Martins, and D. Morichon, 2021: Wave-filtered surf zone circulation under high-energy waves derived from video-based optical systems. *Remote Sens.*, **13**, 1874, https://doi.org/10.3390/rs13101874.

Thielicke, W., and R. Sonntag, 2021: Particle Image Velocimetry for MATLAB: Accuracy and enhanced algorithms in PIVlab. *J. Open Res. Software*, **9**, 12, https://doi.org/10.5334/jors.334.

——, and E. J. Stamhuis, 2014: PIVlab—towards user-friendly, affordable and accurate digital particle image velocimetry in MATLAB. *J. Open Res. Software*, **2**, e30, https://doi.org/10.5334/jors.bl.

Wilson, G. W., H. T. Özkan-Haller, R. A. Holman, M. C. Haller, D. A. Honegger, and C. C. Chickadel, 2014: Surf zone bathymetry and circulation predictions via data assimilation of remote sensing observations. *J. Geophys. Res. Oceans*, **119**, 1993–2016, https://doi.org/10.1002/2013JC009213.